Volume 7 | Number 15 | 21 April 2019 | Pages 4271–4596

Journal of Materials Chemistry C

Materials for optical, magnetic and electronic devices

rsc.li/materials-c

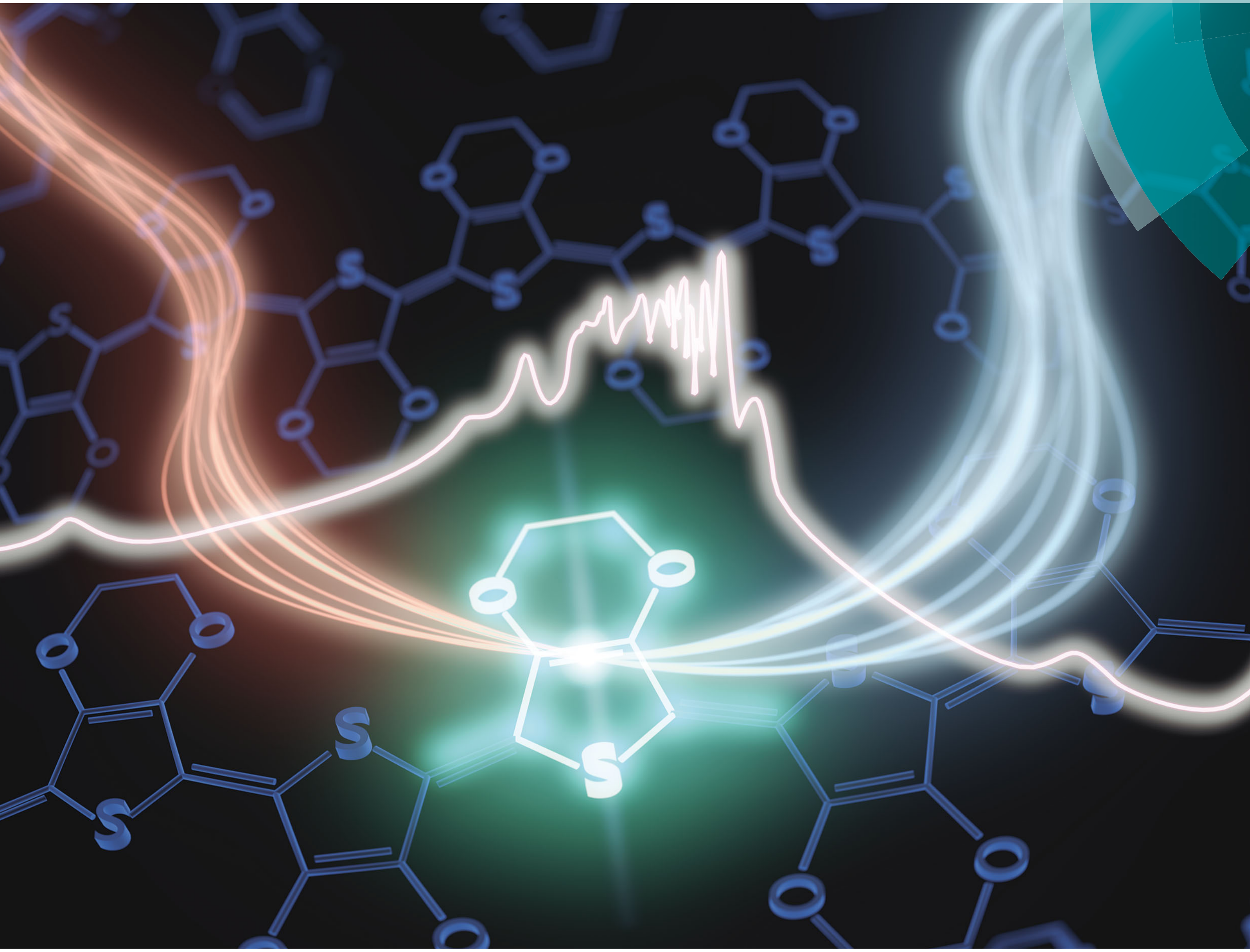

ISSN 2050-7526

ROYAL SOCIETY OF CHEMISTRY | Celebrating IYPT 2019

PAPER

Vanya Darakchieva, Magnus P. Jonsson *et al.*

On the anomalous optical conductivity dispersion of electrically conducting polymers: ultra-wide spectral range ellipsometry combined with a Drude–Lorentz model

Journal of
Materials Chemistry C

PAPER

View Article Online
View Journal | View Issue

Check for updates

Cite this: *J. Mater. Chem. C*, 2019, 7, 4350

On the anomalous optical conductivity dispersion of electrically conducting polymers: ultra-wide spectral range ellipsometry combined with a Drude–Lorentz model†

Shangzhi Chen,[a] Philipp Kühne,[b] Vallery Stanishev,[b] Sean Knight,[c]
Robert Brooke,[d] Ioannis Petsagkourakis,[a] Xavier Crispin,[a]
Mathias Schubert,[bce] Vanya Darakchieva*[b] and Magnus P. Jonsson*[a]

Electrically conducting polymers (ECPs) are becoming increasingly important in areas such as optoelectronics, biomedical devices, and energy systems. Still, their detailed charge transport properties produce an anomalous optical conductivity dispersion that is not yet fully understood in terms of physical model equations for the broad range optical response. Several modifications to the classical Drude model have been proposed to account for a strong non-Drude behavior from terahertz (THz) to infrared (IR) ranges, typically by implementing negative amplitude oscillator functions to the model dielectric function that effectively reduce the conductivity in those ranges. Here we present an alternative description that modifies the Drude model *via* addition of positive-amplitude Lorentz oscillator functions. We evaluate this so-called Drude–Lorentz (DL) model based on the first ultra-wide spectral range ellipsometry study of ECPs, spanning over four orders of magnitude: from 0.41 meV in the THz range to 5.90 eV in the ultraviolet range, using thin films of poly(3,4-ethylenedioxythiophene):tosylate (PEDOT:Tos) as a model system. The model could accurately fit the experimental data in the whole ultrawide spectral range and provide the complex anisotropic optical conductivity of the material. Examining the resonance frequencies and widths of the Lorentz oscillators reveals that both spectrally narrow vibrational resonances and broader resonances due to localization processes contribute significantly to the deviation from the Drude optical conductivity dispersion. As verified by independent electrical measurements, the DL model accurately determines the electrical properties of the thin film, including DC conductivity, charge density, and (anisotropic) mobility. The ellipsometric method combined with the DL model may thereby become an effective and reliable tool in determining both optical and electrical properties of ECPs, indicating its future potential as a contact-free alternative to traditional electrical characterization.

Received 13th December 2018,
Accepted 19th March 2019

DOI: 10.1039/c8tc06302h

rsc.li/materials-c

1. Introduction

Since the discovery of the first conjugated polymer in 1977, there has been tremendous progress in the field of electrically conducting polymers (ECPs), both at the fundamental level and in terms of practical applications.[1–5] Owing to their intriguing physical properties, modern ECPs, such as polyaniline, polypyrrole, and polythiophene, are widely used in optoelectronics, biomedical systems, and renewable energy devices.[2,6–9] Tuning and improving their properties *via* chemical or electrochemical doping further enables meeting the requirements for applications like (commercialized) transparent electrodes.[10,11]

Charge transport in ECPs is related to local polaronic charges situated along the polymer backbone. Thermally-assisted hopping of these polaronic species between neighboring polymer chains then facilitates macroscopic electrical conductivity in the material.[4,12] The polarons are relatively well understood in terms of energy levels, spin and DC transport.[13] However, there are controversies regarding suitable models to describe the materials' AC behavior and extension to optical conductivity,

---

[a] *Laboratory of Organic Electronics, Department of Science and Technology (ITN), Linköping University, SE-601 74 Norrköping, Sweden. E-mail: magnus.jonsson@liu.se*
[b] *Terahertz Materials Analysis Center, Department of Physics, Chemistry and Biology (IFM), Linköping University, SE-581 83 Linköping, Sweden. E-mail: vanya.darakchieva@liu.se*
[c] *Department of Electrical and Computer Engineering, University of Nebraska-Lincoln, Lincoln, Nebraska, 68588-0511, USA*
[d] *RISE Acreo, SE-601 74 Norrköping, Sweden*
[e] *Leibniz-Institut für Polymerforschung Dresden e.V., 01069 Dresden, Germany*

† Electronic supplementary information (ESI) available. See DOI: 10.1039/c8tc06302h

which is tightly connected to transport properties in combination with vibrational resonances.[3,14–17]

The complex-valued optical conductivity (σ) is interconnected with the permittivity or dielectric function (ε) of the material *via*:[18,19]

$$\sigma(\omega) = \mathrm{i}\varepsilon_0\omega[\varepsilon_\infty - \varepsilon(\omega)], \qquad (1)$$

where ε_∞ is the permittivity offset at high frequencies (beyond the measurement limits), i is the imaginary unit, ε_0 is the vacuum permittivity, and ω is the angular frequency.[18] The frequency dependent permittivity dispersion is commonly derived from reflectivity measurements (for UV to IR ranges).[14,20–25] This approach involves integration over all frequencies *via* Kramers–Kronig transformation and therefore requires assumptions of the optical behavior beyond the experimental frequency range.[24] In turn, the obtained permittivity dispersion is sensitive to details of these extrapolated data, especially at lower frequencies approaching zero. Small differences in the extrapolation parameters might therefore lead to significantly different interpretations of the optical behavior of the same material.[26–29] In addition, thin films of ECPs are often highly anisotropic, while commonly employed reflectance and transmittance measurements are based on normal incident light and only provide information for the electric field polarization parallel to the substrate surface.

Spectroscopic ellipsometry (SE) is a well-established precise, and sensitive method for characterizing optical properties of materials.[15,30–34] By measuring polarization changes of reflected (or transmitted) light at oblique incident angles, the material properties can be accurately determined through a best-fit permittivity (optical conductivity) model, without need for Kramers–Kronig transformation and related extrapolations.[15,30,35] SE can provide information on various material properties, such as optical anisotropy, interband transitions, and vibrational resonances.[31–34] Depending on the physical model used, the best-fit model parameters can also be used to determine electrical properties, such as DC conductivity, charge density, and anisotropic mobility. The main limitation in applying this approach for ECPs is that there is no widely accepted optical conductivity model that account for all features of the materials, including the anomalous non-Drude behavior at low frequencies. In turn, physical parameters (*e.g.* charge density, mobility) obtained using different proposed models can vary significantly and deviate from values obtained by direct electrical characterizations.[36–39] We also note that a non-Drude behavior might occur in the far infrared (FIR) or even in the THz range, which until recently was beyond the reach of state-of-the-art ellipsometry instrumentation.[40] Recent progress in frequency-domain THz technology (*e.g.* backward wave oscillator light sources) now enable SE down to 0.1 THz.[40–42] THz and FIR ellipsometers, combined with their counterparts in higher energy ranges, make it possible to investigate material properties in an ultra-wide spectral range.[43] To our best knowledge, ECPs have not previously been investigated by SE in a wide spectral range including the THz and FIR regions.

Here, we investigate the permittivity and optical conductivity of ECPs using ultra-wide spectral range ellipsometry (UV to THz range). The ellipsometric data were acquired using custom-built THz and FIR ellipsometers,[40] combined with their counterparts in the ultraviolet-visible-near infrared (UV-Vis-NIR) and mid-infrared (MIR) ranges. As model ECP system, we use thin films of poly[3,4-ethylenedioxythiophene] (PEDOT), which is the most widely used ECP for organic electronic devices, owing to its attractive optical and electrical properties.[16,22,36,44–53] More specifically, we employed vapor phase polymerization (VPP) to synthesize thin films of highly conductive PEDOT:tosylate (PEDOT:Tos, where tosylate is the counterion balancing the charge).[54] VPP PEDOT:Tos typically has a high degree of order and has been reported to exhibit semi-metallic behavior, making it further more attractive for a comprehensive frequency-dependent optical conductivity study.[20,49]

Suitable optical conductivity models for PEDOT and other ECPs have been long debated without reaching consensus. Instead of the widely used Drude Smith (DS) model[17] and localization-modified Drude (LMD) model,[14,23] both of which we will briefly recall below, we employ a model based only on a Drude term and multiple positive-amplitude Lorentz oscillators. This Drude–Lorentz (DL) model shows an excellent fit to the ellipsometric data and reproduces the fine features in the full spectral range. In turn, this allows us to reveal for the first time the optical conductivity and permittivity dispersions of an ECP in the ultra-wide spectral range from UV to THz. Detailed analysis of the optical conductivity enables identification of interband transitions, molecular vibrations, localization effects, and optical anisotropy of the PEDOT:Tos thin film. We find that vibrational resonances, rarely accounted for in studies of ECPs,[22–24] contribute significantly to the overall non-Drude optical conductivity behavior of the PEDOT:Tos film. As verified by independent electrical measurements, the combined ultrawide SE and DL model approach provides accurate values for the electrical properties of the material, including electrical DC conductivity, charge carrier density, and (anisotropic) mobility. This illustrates that the methodology could be used as a non-contact and damage-free methodology for characterizing optical and electrical properties of ECPs. By varying a few fit parameters, the DL model could easily be applied to PEDOT:Tos films of different thicknesses, with good fit to experimental data.

2. Experimental

2.1 Chemicals

CLEVIOS™ C-B 54 V3 (54% wt/wt iron(III) *p*-toluene sulfonate ($Fe(Tos)_3$) in *n*-butanol) was purchased from Heraeus (Germany). EDOT monomer (142.18 g mol^{-1}) and the triblock copolymer poly(ethylene glycol)-*block*-poly(propylene glycol)-*block*-poly(ethylene glycol) (PEG–PPG–PEG) (5800 g mol^{-1}) were purchased from Sigma-Aldrich. All materials were used as received with no further purification.

2.2 Film preparation

PEDOT:Tos films were prepared *via* vapor phase polymerization (VPP) of EDOT monomers in the presence of $Fe(Tos)_3$ within a vacuum chamber. The oxidant solution was prepared by mixing 2 g of C-B 54 V3, 2 g of the triblock copolymer PEG–PPG–PEG, and 5 g of ethanol (99.5 wt%). Films were deposited by spin-coating the oxidant solution at 1500 rpm for 30 s onto glass substrates. After 30 s baking on a hotplate of 70 °C, the samples were transferred into the vacuum chamber. EDOT droplets were drop-casted onto glass substrates on a hot plate of 60 °C inside the chamber to ensure its evaporation. After 30 min (60 min for the thicker films), the samples were taken out from the chamber and baked on a hotplate at 70 °C for 2 min. Then ethanol was used to wash away the unreacted oxidants and monomers, followed by drying with nitrogen. For ellipsometry measurements, PEDOT:Tos films were deposited on 2 inch single side polished *c*-plane sapphire wafers (Semiconductor Wafer Inc., Taiwan) under the same conditions as for the glass substrates.

2.3 Optical characterization

UV-Vis-NIR absorption measurements were performed using a Lambda 900 spectrometer (PerkinElmer) and spectra were recorded from 350 to 2000 nm with steps of 1 nm. For FTIR measurements, the samples were deposited on un-doped double side polished silicon wafers (University Wafer Inc., United States). Equinox 55 spectrometer (Bruker) was used to acquire FTIR spectra of the samples in transmission mode using a resolution of 4 cm^{-1} and 20 scans.

2.4 Electrical and thickness characterization

Sheet resistance, R_s, was measured on the film surface *via* a 4-point probe set-up using a Signatone Pro4 S-302 resistivity stand and a Keithley 2400. Film thickness, t, was measured by a surface Profiler (Dektak 3st Veeco). The conductivity was then calculated using the equation $\sigma = 1/(R_s t)$.

2.5 Electrochemical chronocoulometry

The setup is based on the three-electrode configuration: Metrohm Ag/AgCl (3 M NaCl) double junction reference electrode and a platinum mesh electrode. Measurements were performed at room temperature in acetonitrile solution with 10 mM $LiClO_4$ as supporting electrolyte and measured by a computer-controlled potentiostat (SP200, BioLogic). The PEDOT:Tos samples were deposited on ITO glass substrates. To measure charge density of the PEDOT:Tos film, a constant voltage of −0.35 eV was applied to the sample to expel the tosylate ions from the film and making it neutral without charge carriers (holes). The charge density in the PEDOT:Tos film equals the concentration of tosylate ions, as widely revealed based on X-ray photoelectron spectroscopy and other studies.[44] Therefore, measuring the charge depletion over time until complete de-doping of the film gives the total initial charge carrier density of the film. The charge depletion process was recorded over a timescale of 2 min until the whole system was stable with no more charge being removed from the film.

2.6 Ellipsometry measurements

Ellipsometry data were collected from four different instruments covering a spectral range from 0.41 meV to 5.90 eV. UV-Vis-NIR measurements were performed using a J. A. Woollam Co. RC2® SE for five angles of incidence Φ_A (40°, 50°, 60°, 70°, and 80°) and the spectral range from 0.73 eV to 5.90 eV (from 210 to 1690 nm). IR measurements were performed using a J. A. Woollam IR-VASE for spectral range from 28 meV to 1.0 eV (from 230 to 7813 cm^{-1}), and at two angles of incidence Φ_A (40° and 60°). FIR measurements were performed on an in-house-built rotating-polarizer rotating-analyzer far-infrared ellipsometer at University of Nebraska, Lincoln. The acquired data of four angles of incidence Φ_A (40°, 50°, 60°, and 70°) were in the spectral range from 3.7 meV to 84 meV (from 30 to 679 cm^{-1}). THz measurements in the spectral range from 0.41 meV to 4.1 meV (from 100 GHz to 1 THz) were performed employing the THz ellipsometer at the Terahertz Materials Analysis Center at Linköping University.[40] Three angles of incidence Φ_A (40°, 50° and 60°) were used for THz measurement. All measurements were performed in normal ambient at room temperature. The typical ellipsometry measurement measures the complex reflectance ratio ρ at different frequencies, which can be calculated *via* the formula:

$$\rho = r_p/r_s = \tan(\psi)e^{i\Delta}, \tag{2}$$

where r_p and r_s are the complex Fresnel reflection coefficients for p- (parallel to the incident plane) and s- (perpendicular to the incident plane) polarized light; ψ describes the amplitude ratio change of the two polarizations; and Δ indicates the phase difference between them.[55] These parameters can then be presented using the *NCS* notation ($N = \cos(2\psi)$, $C = \sin(2\psi)\cos(\Delta)$, and $S = \sin(2\psi)\sin(\Delta)$).[34] N, C, and S are interdependent and thus only two of them are sufficient for data interpretation.

2.7 Ellipsometry data analysis

WVASE® software (J. A. Woollam Co.) was used for data analysis. SE data analysis is based on model approaches, where the sample is described by a box model (homogeneous layer approach and modelled using Fresnel reflection or transmission equations and matrix transfer algorithms). Model approaches are then used to render the frequency dependence of the permittivity of the materials constituents within the samples. The models are presented and discussed in Sections 3 and 4.3. A best-match model approach is employed, based on non-linear numerical regression algorithms that determine the best-match between calculated and experimental ellipsometry data by varying model parameters, such as the thickness of the sample and model permittivity parameters. The best-match model approach is obtained when the weighted error function reaches its minimum and the best-match model parameters are reported as the results. The same numerical analysis determines the amount of correlation between best-match model parameters as well as their numerical uncertainty, reported here within the 90% confidence interval. A confidence interval describes the range within which a given best-match model parameter will be found again upon repeating the numerical best-match model calculation procedure. The ultra-wide spectral range ellipsometry data collected from four different instruments were analyzed simultaneously using a single model (see ESI†).

3. Theoretical models and approaches

This section introduces the standard Drude model, discuss different modifications used for ECPs and describe the DL model based on a Drude term and multiple Lorentz oscillators.

3.1 The Drude model

The most basic optical conductivity model for conventional conductors is the Drude model, which has been widely applied to explain the optical properties of metals and inorganic conductors.[56] The Drude model treats the electrons as an incompressible charge fluid with zero resonance energy due to lack of a restoring force. The carriers experience friction upon movement under the influence of a time-varying electric field, which leads to broadening in the dispersion of the frequency dependence of the optical conductivity. Referred to as plasma broadening, the friction can be interpreted as the result of carrier–carrier scattering and/or collisions with molecules, atoms, or ions.[33,56,57] The optical conductivity σ_D and permittivity ε_D in the Drude model are then described by the plasma frequency (ω_p) and the momentum-averaged scattering time (τ),[32,57] alternatively by the charge density (n) and the mobility (μ):

$$\varepsilon_D(\omega) = \varepsilon_\infty - \frac{{\omega_p}^2\tau}{\omega^2\tau + i\omega} = \frac{ne\mu}{\varepsilon_0(\omega^2 m\mu/e + i\omega)}, \tag{3}$$

$$\sigma_D(\omega) = \frac{\varepsilon_0{\omega_p}^2\tau}{1 - i\omega\tau} = \frac{ne\mu}{1 - i\omega m\mu/e}, \tag{4}$$

where e is the elemental charge and m is the effective mass of the charge carriers.[18,57] Fig. S1 (ESI†) exemplifies typical Drude dispersion and its dependence on n and μ. The DC conductivity is defined as the optical conductivity value at zero frequency ($\sigma_D(0) = ne\mu$), which should then be equal to the electrically measured conductivity for the material of interest.

3.2 Previous modifications of the Drude model applied to ECPs

The optical conductivity of most ECPs deviates from Drude behavior in the longer wavelength range, especially in the range of a few to tens of THz.[16,22,25,51] The most striking deviation is the appearance of a peak in the real optical conductivity in the FIR or MIR ranges followed by reduced conductivity for vanishing frequencies (illustrated in Fig. 1(a)). Likewise, two zero-crossing points (instead of only one for the Drude model) have been observed for the real permittivity, forming a minimum in its dispersion curve.[14,17] Modifications of the Drude model to account for these deviations include the LMD model and the DS model.[14,17]

The LMD model considers charge transport to be limited by disorder-induced weak localization effects,[58] with optical conductivity and permittivity described by:[14,23,24]

$$\varepsilon_{\mathrm{LMD}}{}' = \varepsilon_\infty - \frac{{\omega_p}^2\tau^2}{1+\omega^2\tau^2}\left[1 + \frac{C}{(k_F v_F)^2\tau^2}\left(\sqrt{6} - 1 - \sqrt{\frac{3}{\omega\tau}}\right)\right], \tag{5a}$$

$$\varepsilon_{\mathrm{LMD}}{}'' = \frac{{\omega_p}^2\tau}{\omega+\omega^3\tau^2}\left[1 - \frac{C}{(k_F v_F)^2\tau^2}\left(1 - \sqrt{3\omega\tau}\right)\right], \tag{5b}$$

$$\sigma_{\mathrm{LMD}}{}' = \frac{\varepsilon_0{\omega_p}^2\tau^2}{1+\omega^2\tau^2}\left[1 - \frac{C}{(k_F v_F)^2\tau^2}\left(1 - \sqrt{3\omega\tau}\right)\right], \tag{6a}$$

$$\sigma_{\mathrm{LMD}}{}'' = \frac{\varepsilon_0{\omega_p}^2\omega\tau^2}{1+\omega^2\tau^2}\left[1 + \frac{C}{(k_F v_F)^2\tau^2}\left(\sqrt{6} - 1 - \sqrt{\frac{3}{\omega\tau}}\right)\right], \tag{6b}$$

where $\varepsilon_{\mathrm{LMD}}{}'$, $\varepsilon_{\mathrm{LMD}}{}''$, $\sigma_{\mathrm{LMD}}{}'$, and $\sigma_{\mathrm{LMD}}{}''$ are the real and imaginary parts of the permittivity functions and optical conductivity from the LMD model, respectively. C is a universal constant of the order of unity. k_F and v_F correspond to the Fermi wave number and the Fermi velocity, respectively.[14,24] The term $C/(k_F v_F)^2$ represents the effect of spatial charge carrier localization.[14] Typical LMD dispersion curves are shown in Fig. 1(b–e) (see also Fig. S2(a–d), ESI†). Notably, $\varepsilon_{\mathrm{LMD}}{}'$ is divergent and approaches infinity in the long wavelength limit, for all non-zero values of $C/(k_F v_F)^2$.[59–61] Such divergence has been suggested to be related to the metal–insulator transition, but no direct evidence of divergence has been observed at low frequencies.[23] On the contrary, results from THz time-domain spectroscopy (THz-TDS) indicated a relatively flat dispersion in the THz range for highly conductive ECPs.[16,51]

The DS model instead modifies the Drude model by considering successive charge carrier collisions with (immobile) ions.[17] In this model, the carrier velocity after each collision reduces (scales) by a parameter C_n, where n denotes the number of collisions. C_n has to take a negative value between −1 and 0, which implies that these charge carriers are backscattered instead of being scattered along their original direction. Only considering the first backscattering event, the DS model is expressed as:[17]

$$\varepsilon_{\mathrm{DS}}(\omega) = \varepsilon_\infty - \frac{{\omega_p}^2\tau}{(\omega^2\tau + i\omega)}\left[1 + \frac{c_1}{1 - i\omega\tau}\right], \tag{7}$$

$$\sigma_{\mathrm{DS}}(\omega) = \frac{\varepsilon_0{\omega_p}^2\tau}{(1 - i\omega\tau)}\left[1 + \frac{c_1}{1 - i\omega\tau}\right], \tag{8}$$

where C_1 is the backscattering parameter for the first collision. Typical DS dispersion curves are shown in Fig. 1(f–i) (also Fig. S2(e–h), ESI†). A major difference from the LMD model is that the real permittivity of the DS model does not diverge but reaches a plateau and approaches a finite value for vanishing frequencies. The DS model turns back to the Drude model for C_1 equal to zero, indicating no backscattering. In this sense, C_1 could also be related to the proportion of so-called

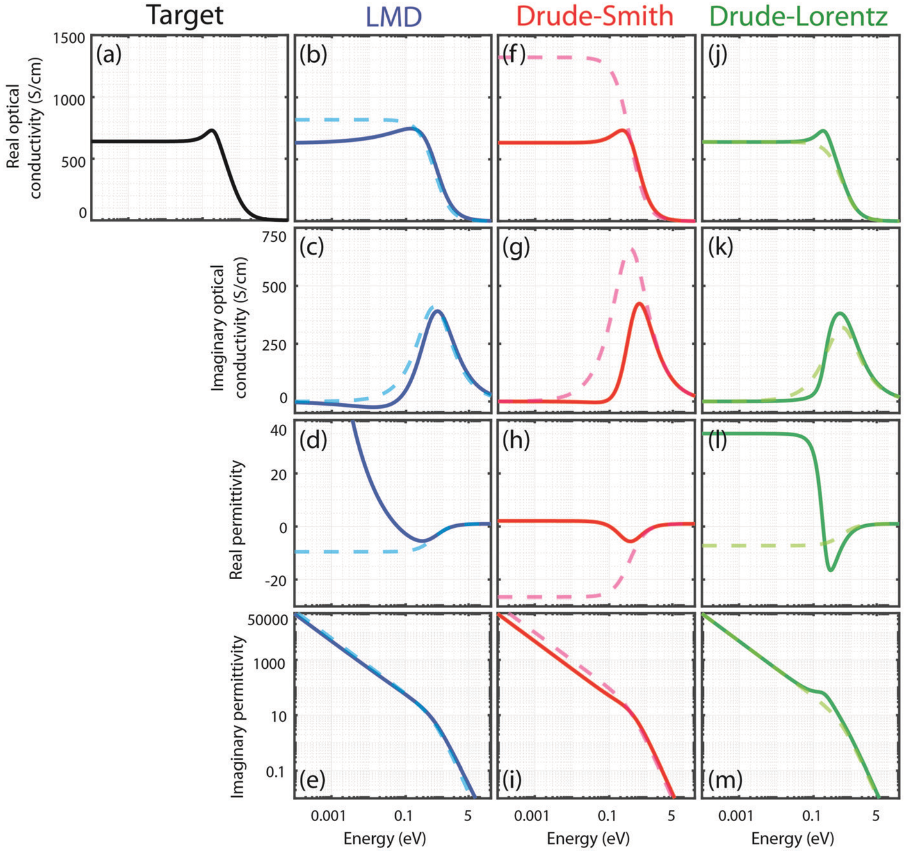

Fig. 1 Schematic example of typical reflectivity measurements of a hypothesized ECP. Conventionally, the real optical conductivity (black solid line in a) can be derived from the measurement using Fresnel equations and Kramers–Kronig transformation together with several assumptions. In the analysis, the real optical conductivity (a) is regarded as a target and three different models are applied to fit for it (LMD: b, DS: f, DL: j). Based on the extracted parameters, their corresponding imaginary optical conductivity (the second row: c, g, and k), real permittivity (the third row: d, h, and l), and imaginary permittivity (the fourth row: e, i, and m) for each model (LMD: blue curves, DS: red curves, and DL: green curves) can be obtained *via* eqn (5–8) and (11, 12). The parameters used for plots are: LMD (ω_p = 2852 THz, γ_p = 879 THz, and $C/(k_F{}^2v_F{}^2)$ = 0.3 fs^2) in blue solid lines, DS (ω_p = 2840 THz, γ_p = 541 THz, and $c_1 = -0.52$) in red solid lines, and DL (ω_p = 2520 THz, and γ_p = 879 THz) with a single molecular vibration resonance positioned at 0.2 eV (amplitude: 1.69 eV^2, and broadening: 0.24 eV) in green solid lines. The contributions from the Drude term in each modified model are indicated by dashed lines. For all the three models, the extrapolated conductivity at zero frequency is about 640 S cm^{-1}.

'backscattered' carriers in the material. However, the exact physical meaning of the parameter C_1 is ambiguous, because it introduces an additional average estimate on carrier scattering probability, which has already been described by the scattering time τ in the original Drude term.[62]

Both the LMD model and the DS model base the optical conductivity on a conductive free charge carrier term (the Drude term, dashed lines in Fig. 1) that is suppressed by modification terms based on negative-amplitude oscillators. As a result, the effective electrical DC mobility and charge density of the material are not represented by the parameters of the Drude term. Since it is not clear how charge density and mobility are individually reduced by the modification terms, it is not straightforward to separately determine these quantities. As example, the DS model has been reported to overestimate charge mobility and underestimate carrier density.[16,51] In addition, neither the LMD nor the DS model account for molecular vibrations, which are important features that contribute to the optical conductivity of organic materials. Although some research implied that molecular vibrations are of minor importance, deviation between experimental data and model fits indicates that not accounting for molecular vibrations may lead to erroneous determination of the charge carrier properties (as the molecular vibration contributions to the optical conductivity may then instead be casted into the carrier transport).[14,22,23,29] It would therefore be valuable to develop a model for the optical conductivity of ECPs that accounts for molecular vibrations and can accurately determine both optical and electrical properties of the material.

3.3 The Lorentz oscillator and the Drude–Lorentz (DL) model

Reflectance and transmittance of ECPs show pronounced spectrally narrow peaks in the infrared (IR) range, which are clear signatures of vibrational modes.[14,22–24] Polar molecular vibrational resonances, related to vibrations or stretching of bonds in the organic materials, contribute to the optical conductivity (and permittivity) in addition to the charge carriers.[19] These resonances can be represented by Lorentz oscillators:[31,32]

$$\varepsilon_{\mathrm{L}}(\omega) = -\frac{A_{\mathrm{L}}}{\omega^2 - \omega_{\mathrm{L}}{}^2 + \mathrm{i}\omega\gamma_{\mathrm{L}}}, \tag{9}$$

$$\sigma_{\mathrm{L}}(\omega) = \frac{\mathrm{i}\varepsilon_0\omega A_{\mathrm{L}}}{\omega^2 - \omega_{\mathrm{L}}{}^2 + \mathrm{i}\omega\gamma_{\mathrm{L}}}, \tag{10}$$

where A_{L}, ω_{L}, and γ_{L} correspond to amplitude, resonance frequency, and broadening, respectively.[15,31,32,34,35,55] Interband transitions (*e.g.* polaronic or bipolaronic absorption bands[49,63]) in the UV-Vis-NIR ranges can also be described by Lorentz oscillators.[15,30] Combining the free charge carrier Drude term with multiple Lorentz oscillators gives the proposed DL model as:[64,65]

$$\varepsilon_{\mathrm{DL}}(\omega) = \varepsilon_{\mathrm{D}}(\omega) - \sum \frac{A_{\mathrm{L}}}{\omega^2 - \omega_{\mathrm{L}}{}^2 + \mathrm{i}\omega\gamma_{\mathrm{L}}}, \tag{11}$$

$$\sigma_{\mathrm{DL}}(\omega) = \sigma_{\mathrm{D}}(\omega) + \sum \frac{\mathrm{i}\varepsilon_0\omega A_{\mathrm{L}}}{\omega^2 - \omega_{\mathrm{L}}{}^2 + \mathrm{i}\omega\gamma_{\mathrm{L}}}. \tag{12}$$

Lorentz oscillators have previously been successfully employed to account for molecular vibrations and interband transitions in ECPs,[15,31] and we here demonstrate that they can also reproduce the anomalous non-Drude behavior of ECPs and thereby provide an alternative description to the LMD and DS models. Fig. 1(j–m) (also Fig. S3, ESI†) show typical dispersion curves for the DL model based on one Drude term and one broad Lorentz oscillator. It is clear that the addition of a single Lorentz oscillator to the Drude term can produce the typical non-Drude behavior observed for ECPs, without leading to any divergences. Furthermore, the contribution from the Drude term to the real optical conductivity (dashed line) is not suppressed at low frequencies as for previous models, but instead directly represents the DC electrical behavior of the material.

Fig. 1 was obtained by first fitting the three models to a 'target' (Fig. 1(a)) in the form of a typical real optical conductivity dispersion for an ECP. The target resembles the commonly obtained results from reflectance measurements. All three models can to good extent reproduce this target. Based on these fits, we then retrieved the corresponding imaginary parts *via* eqn (6), (8), and (12), which show some differences (see Fig. 1(c, g and k)). More drastic differences are found when converting to the real permittivity. Hence, even if all three models can reach an excellent fit for the real optical conductivity, the derived real permittivity and thereby the corresponding model information can be substantially different. This illustrates a common issue for data analysis based on experimental results of only one part of a complex-valued parameter (the real optical conductivity in the example) and retrieving the other part by Kramers–Kronig transformation. In that respect, we note that SE measures two quantities (ψ and Δ) and can directly provide both the real and imaginary parts of the complex-valued optical conductivity *via* fitting to the experimental data. This makes SE highly suitable for characterization of complex optical conductivity and permittivity dispersions.

4. Results and discussion

4.1 Ultra-wide spectral range ellipsometry data analysis for PEDOT:Tos

Fig. 2(a) displays the chemical structure of the chosen model ECP, PEDOT:Tos. The Tos counterion carrying negative charge acts to maintain charge neutrality of the system. Therefore, the concentration of tosylate ions equals the positive charge (hole) density of the PEDOT. We employed SE (schematic illustration of SE measurement is presented in Fig. 2(b)[34]) to measure the real and imaginary parts of the complex-valued reflectance ratio of PEDOT:Tos thin film (thickness measured by profiler to be 180 ± 10 nm), and to derive the optical conductivity (permittivity) by the DL model approach. The four spectral windows for the ultra-wide spectral range ellipsometry are illustrated in Fig. 2(c) as THz (red), FIR (yellow), MIR (green), and UV-Vis-NIR (blue). The experimental SE results are shown as red and blue solid curves in Fig. 2(c).

Initial fitting attempts employed an isotropic DL model, with the best-matched model curves presented in Fig. S4(a) (ESI†). No satisfactory fit could be obtained, with significant deviations from the experimental features in both UV-Vis-NIR and MIR ranges. Optical anisotropy has indeed been reported in the UV-Vis-NIR range for thin PEDOT:Tos films and confirmed by structural characterization.[15,66] We found that the anisotropy is also crucial for the MIR range, where most previous studies treated PEDOT films as isotropic.[31,32] Based on this finding, we introduced a uniaxial anisotropic model with two directions: in-plane (or ordinary axis, parallel to the sample surface) and out-of-plane (or extraordinary axis, normal to the sample surface). At wavelengths beyond MIR we treated the film as isotropic due to limited sensitivity to the out-of-plane component in the FIR and THz ranges. We further required the Drude term's carrier density n to be the same for both axes, while allowing the mobility μ to be different. By implementing several different Lorentz oscillators (including interband transitions in UV-Vis-NIR and molecular vibration resonances in MIR), the best-match calculated model exhibits excellent fit to the experimental data (grey dotted curves in Fig. 2(c)). The anisotropic DL model can reproduce all the fine features of the experimental curves in the UV-Vis-NIR and MIR ranges. The strong oscillating features of both N and C at the FIR boundary towards the THz range (between 4.1 meV to 20 meV) are caused by incompletely spectrally resolved Fabry–Perot interferences within the sapphire substrate. The interference pattern becomes more clearly resolved in the THz range. The film thickness obtained from the SE fit (189 ± 1 nm) agrees with the thickness measured by profilometry (180 ± 10 nm).

The validity of the anisotropic DL model was further confirmed by applying it to the SE data analysis of another PEDOT:Tos thin film prepared in an identical way but with different thickness (polymerization duration). Keeping the

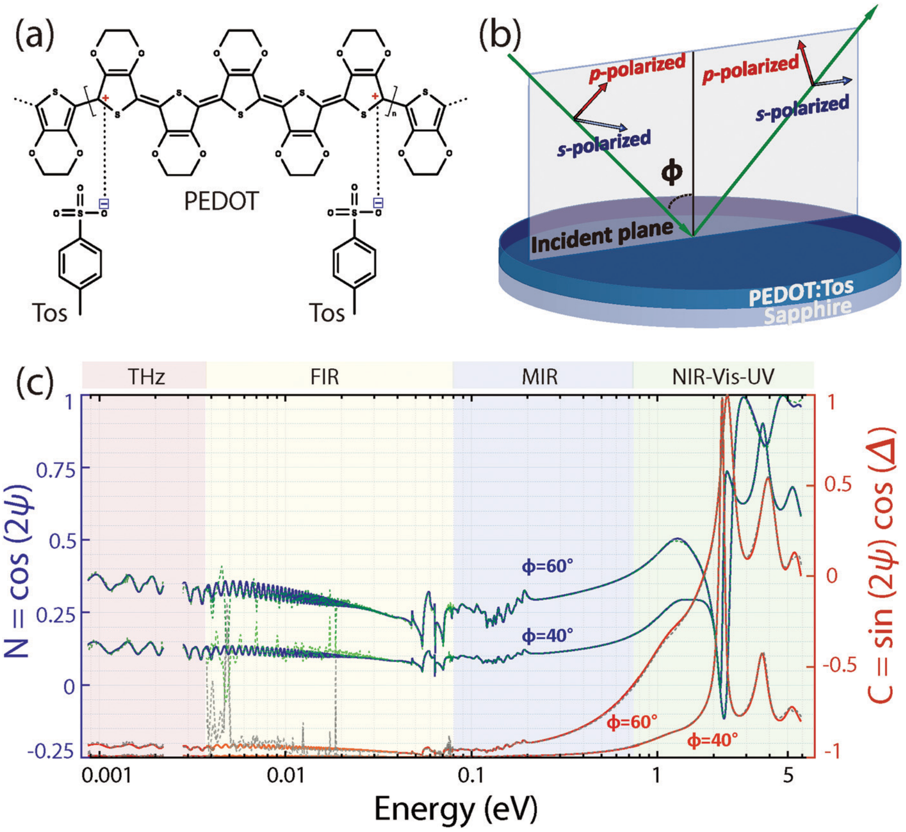

Fig. 2 (a) The chemical structure of PEDOT and Tos ions. (b) Schematic illustration of SE measurements. (c) Ellipsometric data (blue and red solid lines) $N = \cos(2\psi)$ and $C = \sin(2\psi)\cos(\Delta)$ of a PEDOT:Tos thin film and best-match model calculated data (gray dotted lines) using the proposed DL model. Four different spectral windows from UV to THz (0.41 meV to 5.9 eV) and two incident angles (40° and 60°) were plotted in the figure. The features at the FIR boundary towards the THz range (between 4.1 meV to 20 meV) are caused by incompletely spectrally resolved Fabry–Perot interferences within the sapphire substrate.‡ The interference pattern is then clearly resolved in the THz range. Ellipsometric data for additional incident angles can be found in Fig. S6 (ESI†).

Lorentz oscillators fixed and only varying the Drude parameters and thickness could directly provide a good fit (see Fig. S7(a), ESI†). Varying the amplitudes and broadenings of some of the Lorentz oscillators further improved the results to an excellent fit (Fig. S7(b), ESI†). Indeed, such modifications are expected based on variations in the polymerization kinetics between films with different thicknesses. As for the thin film, the thickness obtained from the model (316 ± 3 nm) agrees with the thickness measured with a profilometer (310 ± 10 nm).

Fig. 3 presents the optical conductivity and permittivity dispersions of the thin PEDOT:Tos film obtained from the best-match calculated DL model results (green curves), for both in-plane and out-of-plane directions. The model correctly reproduces the well-known non-Drude features of ECPs, including the real optical conductivity peak and the two zero crossings for the real permittivity. For comparison, we also present results obtained using the LMD (blue curves) and DS (red curves). For these two models, molecular vibrations were not included, while we implemented interband transitions in a similar way as for the DL model (the Lorentz oscillators in UV-Vis-NIR range). As expected, the three models show similar overall behavior for the in-plane real optical conductivity (Fig. 3(a)). This means that the Lorentz oscillators positioned in the MIR range for the DL model produce a similar non-Drude peak as the other two models, but with more fine features originating from contribution of spectrally narrow molecular vibrational resonances. We also identify a real optical conductivity peak in the THz range for the DL model, implying the existence of weakly localized charge carriers. This also leads to a clear feature in the real permittivity dispersion (Fig. 3(c)).

We note that the real permittivity dispersion obtained from the DL model, derived from the excellent fit of the ellipsometric data in the THz range (see Fig. 2(c)), shows no trend of divergence. After the expected increase in the MIR range for decreasing frequencies (producing the 2nd zero crossing), the real permittivity reaches a plateau and approaches a constant finite value for lower frequencies (see Fig. 3(c)). This result is in agreement with findings from THz-TDS measurements of similar material systems.[51]

Besides Lorentz oscillators accounting for anisotropic interband transitions in the UV-Vis-NIR range, several in-plane and out-of-plane oscillators were required to accurately capture the

---

‡ Please note that polar gas molecules present in the beam path can cause rotational–vibrational absorption lines and thus decrease the signal-to-noise ratio in narrow parts of the spectral range, causing sharp features in the experimental data.

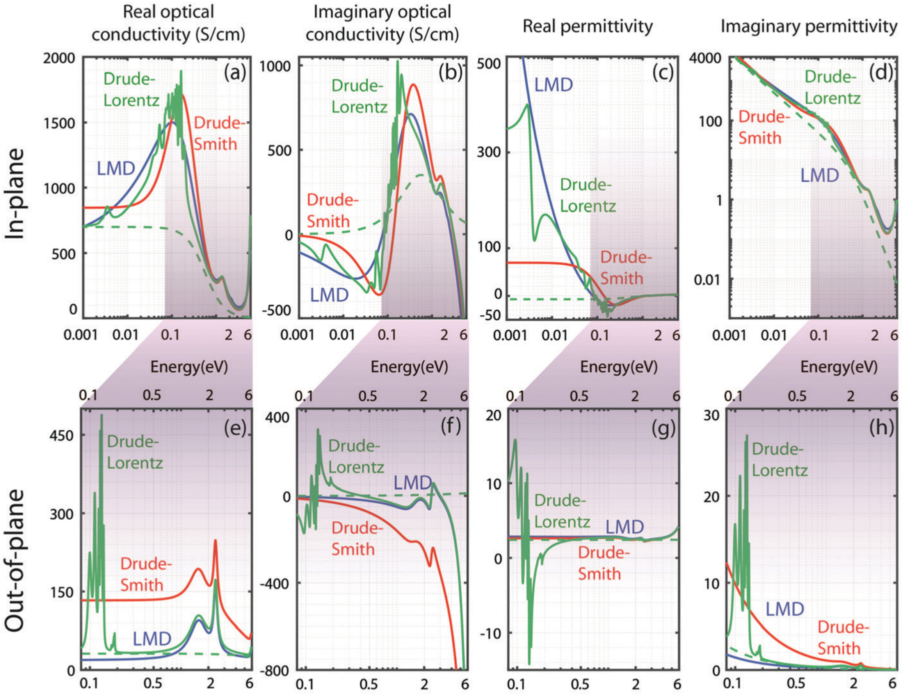

Fig. 3 The optical conductivity (real part: a, e; imaginary part: b, f) and permittivity dispersions (real part: c, g; imaginary part: d, h) of PEDOT:Tos thin film derived from three different models: LMD (blue solid lines), DS (red solid lines), and DL (green solid lines). The Drude contribution in DL model is demonstrated by the green dashed lines. In both LMD and DS model, several Lorentz oscillators representing interband transitions are added to get a better fitting in UV-Vis ranges. The top panel (a–d) displays the information from the in-plane axis and the bottom panel (e–h) shows the out-of-plane information. The out-of-plane components of the optical conductivity and permittivity are given only for the spectral range from 84 meV to 5.9 eV, for which the SE data possess sensitivity to the optical anisotropy. For the spectral range from 0.41 meV to 84 meV the out-of-plane components of the optical conductivity and permittivity are identical to their respective in-plane counterparts and thus omitted in (e–h).

anisotropy in the MIR range, especially to account for the spectrally narrow features between 0.15 eV to 0.25 eV (Fig. 2(c) and Fig. S5, ESI†). These vibrational resonances contribute significantly to the anisotropic optical conductivity and permittivity, which is not captured by the simplified models without molecular vibrations. Comparing the in-plane and out-of-plane real optical conductivity (Fig. 3(a and e)) or real permittivity (direct comparison is presented in Fig. S4(b), ESI†), we find substantial differences. Along the out-of-plane direction the PEDOT:Tos acts as a dielectric with a flat and almost constant curve topped with several resonance features due to interband transitions and molecular vibration resonances. By contrast, a significant conductivity of the PEDOT:Tos is revealed in the in-plane direction. We finally note that the permittivity dispersion derived from the isotropic DL model is, despite the worse fit, similar to the in-plane permittivity obtained from the anisotropic DL model (Fig. S4(b and c), ESI†). This could be due to the lower experimental sensitivity for the out-of-plane direction (only the vertical component of the p-polarized light can probe the out-of-plane direction as indicated in Fig. 2(b)). Even with multiple incident angles,[34] the extraordinary direction has less impact on the overall optical properties of the system.

4.2 Comparison of extracted parameters with independent electrical measurements

We performed independent electrical measurements to evaluate the accuracy and reliability of values extracted from the SE data analysis using the three different models. We also applied the DS model to a more limited spectral range from 0.2 to 3 THz to resemble typical application of the DS model to THz-TDS data[16,51] (denoted DS-THz in Table 1 and the results are shown in Fig. S8, ESI†). All results are summarized in Table 1. As detailed in the Experimental section, we measured in-plane conductivity by the 4-point probe method and charge density by electrochemical chronocoulometry (see Fig. S9, ESI†). The ratio between in-plane conductivity and charge density then gives the in-plane mobility. These values are presented as ‘Electrical’ in Table 1 and they agree well with values reported in literature (see Table S1, ESI†). From the SE results, the DC conductivity was determined from the real optical conductivity at zero frequency, *via* eqn (6a), (8), and (12) using the best-match parameters of the four model fits. The DC Drude conductivity (σ_D) was calculated as the real optical conductivity of the respective Drude component at zero frequency. We further introduce a modification ratio parameter A to describe the ratio between the DC conductivity and DC Drude conductivity. The DL model directly gives the effective DC conductivity $\sigma(0)$ as $\sigma_D(0)$, while the other models require application of the modification ratio A on $\sigma_D(0)$ to obtain the effective material properties.

We first note that all four models give in-plane DC conductivity values that are within the uncertainty range of the electrically measured value of 670 ± 50 S cm^{-1}, although the DL

Table 1 Electrical measurement and fit parameters based on the different models: the charge density, the charge mobility, the DC Drude conductivity, modification coefficient of the Drude model, and the DC conductivity of PEDOT:Tos thin films. DS-THz stands for the DS model only applied within 0.2 to 3 THz range. Modification *A* is a parameter describing the fraction of DC Drude conductivity that is retained after modifications from different models

		Electrical	DL	LMD	DS	DS-THz
In-plane	DC conductivity (S cm^{-1})	670 ± 50	700 ± 3	585 ± 170	787 ± 70	690 ± 240
	Mobility ($\mathrm{cm}^2\ \mathrm{V}^{-1}\ \mathrm{s}^{-1}$)	1.96 ± 0.25	1.99 ± 0.007	5.16 ± 0.41	6.18 ± 0.03	125.2 ± 18.8
	Modification ratio *A*		1	0.36 ± 0.05	0.24 ± 0.02	0.53 ± 0.04
	DC Drude conductivity (S cm^{-1})		700 ± 3	1626 ± 210	3282 ± 40	1302 ± 340
Out-of-plane	DC conductivity (S cm^{-1})		32 ± 2	25 ± 50	129 ± 110	
	Mobility ($\mathrm{cm}^2\ \mathrm{V}^{-1}\ \mathrm{s}^{-1}$)		0.09 ± 0.004	0.08 ± 0.15	0.26 ± 0.15	
	Modification ratio *A*		1	0.99 ± 0.01	0.94 ± 0.53	
	DC Drude conductivity (S cm^{-1})		32 ± 2	25 ± 50	138 ± 80	
Charge density ($10^{21}\ \mathrm{cm}^{-3}$)		2.13 ± 0.13	2.20 ± 0.002	1.97 ± 0.10	3.32 ± 0.02	0.065 ± 0.007

model is closest and shows significantly smaller error bar. Turning to charge density and mobility, we observe stronger differences between the models. The charge density obtained from the DL model ($2.20 \pm 0.002 \times 10^{21}\ \mathrm{cm}^{-3}$) agrees very well with the electrically measured value ($2.13 \pm 0.13 \times 10^{21}\ \mathrm{cm}^{-3}$). The slightly lower electrical value may be due to the fact that the electrochemical characterization is applied to the whole area of the sample, also including less conductive and/or defective regions around the edges. The in-plane mobility predicted by the DL model ($1.99 \pm 0.007\ \mathrm{cm}^2\ \mathrm{V}^{-1}\ \mathrm{s}^{-1}$) exhibits a value almost identical to the one obtained from the electrical measurements ($1.96 \pm 0.25\ \mathrm{cm}^2\ \mathrm{V}^{-1}\ \mathrm{s}^{-1}$). Hence, the DL model provides accurate values of charge density and mobility of the sample, without need for modification factors.

It is less straightforward to extract DC mobility and charge density for the LMD and the DS models. The reason is that these quantities originate from the respective Drude terms, which for those models do not describe the effective DC electrical properties of the material. While the DC conductivity can be obtained by multiplication with *A*, it is less clear how the charge density and mobility are individually modified from the Drude parameters. Evaluating the non-modified values, the charge density obtained from the LMD model ($1.97 \pm 0.10 \times 10^{21}\ \mathrm{cm}^{-3}$) is relatively close to the experimental value while the DS model shows larger difference ($3.32 \pm 0.02 \times 10^{21}\ \mathrm{cm}^{-3}$). Regarding mobility, both the LMD model ($5.16 \pm 0.41\ \mathrm{cm}^2\ \mathrm{V}^{-1}\ \mathrm{s}^{-1}$) and the DS model ($6.18 \pm 0.03\ \mathrm{cm}^2\ \mathrm{V}^{-1}\ \mathrm{s}^{-1}$) provide values that are much higher than the electrically obtained mobility. However, assuming that the modification parameter *A* acts only on the mobility and not on the charge density gives a good agreement for both parameters for the LMD model, while both parameters are inaccurate for the DS model. It should be stressed that the error bars extracted from the DL model are much smaller compared to the error bars obtained from the LMD and DS models. The results illustrate the value of the DL model in terms of providing non-modified parameters that directly correspond to the electrically measured values at high precision.

We introduce anisotropy ratio as the quotient of the in-plane DC conductivity and the out-of-plane DC conductivity. The calculated ratio from the DL model demonstrates a pronounced anisotropy with a ratio of 20. This is in good agreement with reported values (see Table S1, ESI†) for PEDOT based materials.[67–69] The LMD model predicts similar behavior (although with less certainty), while the DS model predicts an anisotropy of only 5.7 (with a very high uncertainty).

We finally note that restricting the spectral range for the DS model to the THz range ('DS-THz' in Table 1) leads to underestimated carrier density and highly overestimated mobility (more mobile than most inorganic semiconductors) even though the best-match model curves (Fig. S7, ESI†) show a good fit to the experimental data in the limited range. These errors are related to inaccurate estimation of ε_∞ from not accounting for the strong frequency-dependence beyond the THz range. We also note that restricting the spectral range to the UV-Vis-NIR could also provide good fits, but with large variations in determined electrical properties. This highlights the importance of applying the model fitting in a wide spectral range (here UV-THz) to extract accurate parameters. We conclude that ultra-wide spectral range ellipsometry in combination with the DL model forms a powerful methodology for non-destructive and non-contact accurate measurement of optical and electrical properties of ECPs.

4.3 Separating contributions from different processes to the optical conductivity

We will now discuss the optical conductivity and permittivity in more detail based on the results from the DL model. From the best-match calculated parameters, we identified 37 in-plane and 14 out-of-plane Lorentz oscillators, as presented for the in-plane direction in Fig. 4(a and b) together with their contributions to the optical conductivity (the contribution from the Drude term was removed for clarity). The amplitude, broadening, and resonance energy (frequency) for each Lorentz oscillator are indicated in Fig. 4(c and d).

Information on interband transitions are provided by the oscillators in the UV-Vis-NIR range, where we find three in-plane transitions as well as two out-of-plane transitions (see Table S2, ESI†). The positions of the in-plane oscillators agree with UV-Vis-NIR absorbance measurements (see Fig. S10(a), ESI†) and also with reported transitions occurring in PEDOT materials (see details in ESI†).[63,70]

Turning to the molecular vibrations, they are identified as spectrally narrow resonances in the MIR and FIR ranges (grey in

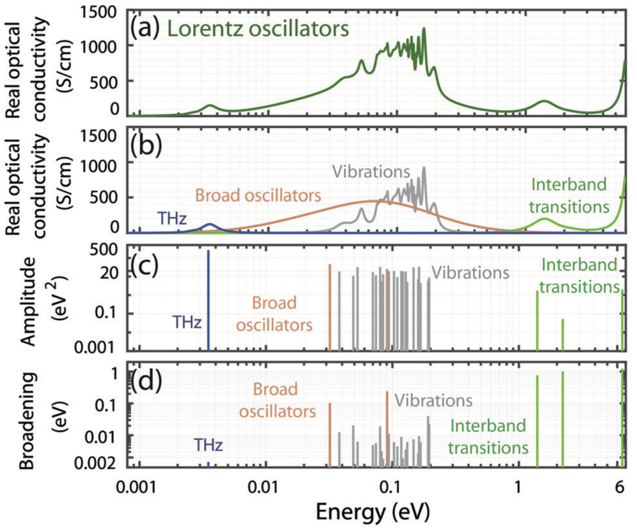

Fig. 4 (a) In-plane real optical conductivity dispersion of PEDOT:Tos represented by multiple Lorentz oscillators (the Drude contributions are removed) derived from the DL model. (b) The contributions of the real optical conductivity from THz (blue curve), broad oscillators (brown curve), interband transitions (green curve), and molecular vibrations (grey curves) are indicated. (c and d) Display the amplitude and broadening parameters for each Lorentz oscillator as well as their resonance energy (frequency). Their out-of-plane counterparts are shown in Fig. S10 (ESI†). The parameters for these Lorentz oscillators are listed in Table S2 (ESI†).

Fig. 4). Several resonances can be assigned to different vibrational modes of the chemical bonds in the polymer film, as indicated also by FTIR spectra (see Fig. S10(b), ESI†). The oscillators located between 0.17 to 0.20 eV can be attributed to symmetrical/asymmetrical stretching modes of C–C or C=C bonds in the thiophene rings (quinoid or benzoid form).[69] Lorentz oscillators at around 0.16 eV (1256 cm^{-1}) are considered as C–C inter-ring stretching in-plane modes.[70] The stretching modes of the alkylenedioxy group (1197, 1063, 1030, and 920 cm^{-1}) can be found in oscillators located in the range of 0.11 to 0.15 eV.[71] Vibrational modes at around 0.085 eV, 0.12 eV, and 0.14 eV correspond to C–S–C stretching (699 and 840 cm^{-1}), ethylenedioxy ring deformation (970 cm^{-1}), and C–O stretching (1098 cm^{-1}), respectively.[70] The absorption bands at 522 and 579 cm^{-1} in FTIR spectra (Fig. S10(b), ESI†) are associated with the Lorentz oscillators at 0.05 to 0.07 eV, indicating the C–O–C bond deformation.[70] We stress that these molecular vibration modes collectively contribute significantly to the overall real optical conductivity, on their own forming a clear peak that resembles non-Drude behavior of ECPs. In that respect, neglecting vibrational modes and instead parameterizing the fitted curves to capture only the overall broad envelope of the experimental data (*i.e.* the optical conductivity peak at low frequencies) can overestimate the non-Drude behavior originating from other mechanisms.[14,20–25]

While most Lorentz oscillators located in the MIR and FIR ranges can directly be considered as molecular vibration resonances (confirmed by FTIR, see Fig. S10(b), ESI†), we also identify oscillators with comparatively larger broadening (indicated by brown lines in Fig. 4(b–d)) that cannot be regarded as single vibrational resonances. One option would be that they originate from the combination of multiple closely spaced molecular vibration resonances with similar amplitude or other localized charge processes with broader energy distribution. Hwang *et al.* studied the IR reflectance spectrum of PEDOT:ClO_4^- with different doping level and analyzed their real optical conductivity dispersion.[65] In their work, they tuned the optical conductivity by reducing the doping level of the system and find that the molecular vibration peaks remained with reduced intensities, while the broad features disappeared together with the Drude background. This suggests that the broad features are not molecular vibrations, but related to charge transport. The Drude term and the broad Lorentz oscillators thereby together represent the effective envelope originating from polaronic charge transport behavior in the material, which could be thought of as a charge transport function. In turn, the possibility to determine the charge transport function with our methodology may be valuable in gaining better understanding of the relation between polaronic hopping transport and optical conductivity in these systems.

Finally, we identify one Lorentz oscillator in the THz range with characteristic energy of 3.5 meV. This feature may be related to low-frequency molecular phonon modes[71] or a signature of localized charge transport,[72] although further studies are needed to exclude influences from this resonance being spectrally close to the transition between the MIR and THz instruments.

5. Conclusion

In summary, we present the anisotropic optical conductivity and permittivity of highly conductive PEDOT:Tos thin films in the ultrawide spectral range from 0.41 meV to 5.9 eV. This is based on spectroscopic ellipsometry and fitting to a Drude–Lorentz (DL) model that accounts for both molecular vibrations and non-Drude charge transport. We find that molecular vibrations play an important role for the correct interpretation of the optical conductivity and permittivity dispersion, contributing significantly to the overall non-Drude behavior. Moreover, the DL model, combined with the ultrawide spectral range ellipsometry, is proven to be an effective approach for also determining the (anisotropic) electrical properties of thin conductive polymer films, with high precision and accuracy. By only tuning thickness and Drude component, the model could easily be applied to different PEDOT:Tos samples. In summary, the combination of the DL model with spectroscopic ellipsometry forms a powerful tool for non-contact and damage-free approach for accurate optical and electrical characterization.

Conflicts of interest

The authors declare no conflicts of interest.

Acknowledgements

We thankfully acknowledge financial support from the Swedish Research Council, the Swedish Foundation for Strategic

Research, the Wenner-Gren Foundations, and the Swedish Government Strategic Research Area in Materials Science on Functional Materials at Linköping University (Faculty Grant SFO-Mat-LiU No. 2009 00971).

References

1 C. K. Chiang, C. R. Fincher Jr, Y. W. Park, A. J. Heeger, H. Shirakawa and E. J. Louis, *et al.*, Electrical conductivity in doped polyacetylene, *Phys. Rev. Lett.*, 1977, **39**(17), 1098.

2 G. Yu, J. Gao, J. C. Hummelen, F. Wudl and A. J. Heeger, Polymer photovoltaic cells: enhanced efficiencies *via* a network of internal donor-acceptor heterojunctions, *Science*, 1995, **270**(5243), 1789–1791.

3 A. J. Heeger, Semiconducting and metallic polymers: the fourth generation of polymeric materials (Nobel lecture), *Angew. Chem., Int. Ed.*, 2001, **40**(14), 2591–2611.

4 J. L. Bredas and G. B. Street, Polarons, bipolarons, and solitons in conducting polymers, *Acc. Chem. Res.*, 1985, **18**(10), 309–315.

5 H. Klauk, *Organic electronics: materials, manufacturing, and applications*, John Wiley & Sons, 2006.

6 D. T. Simon, E. O. Gabrielsson, K. Tybrandt and M. Berggren, Organic bioelectronics: bridging the signaling gap between biology and technology, *Chem. Rev.*, 2016, **116**(21), 13009–13041.

7 J. Y. Oh, S. Rondeau-Gagné, Y.-C. Chiu, A. Chortos, F. Lissel and G.-J. N. Wang, *et al.*, Intrinsically stretchable and healable semiconducting polymer for organic transistors, *Nature*, 2016, **539**(7629), 411.

8 F. Croce, G. B. Appetecchi, L. Persi and B. Scrosati, Nanocomposite polymer electrolytes for lithium batteries, *Nature*, 1998, **394**(6692), 456.

9 M. Berggren, O. Inganäs, G. Gustafsson, J. Rasmusson, M. R. Andersson and T. Hjertberg, *et al.*, Light-emitting diodes with variable colours from polymer blends, *Nature*, 1994, **372**(6505), 444.

10 P. M. McManus, S. C. Yang and R. J. Cushman, Electrochemical doping of polyaniline: effects on conductivity and optical spectra, *J. Chem. Soc., Chem. Commun.*, 1985, **22**, 1556–1557.

11 A. O. Patil, A. J. Heeger and F. Wudl, Optical properties of conducting polymers, *Chem. Rev.*, 1988, **88**(1), 183–200.

12 C. Yoon, M. Reghu, D. Moses, A. Heeger, Y. Cao and T.-A. Chen, *et al.*, Hopping transport in doped conducting polymers in the insulating regime near the metal-insulator boundary: polypyrrole, polyaniline and polyalkylthiophenes, *Synth. Met.*, 1995, **75**(3), 229–239.

13 I. Zozoulenko, A. Singh, S. K. Singh, V. Gueskine, X. Crispin and M. Berggren, Polarons, Bipolarons, And Absorption Spectroscopy of PEDOT, *ACS Appl. Polym. Mater.*, 2018, **1**(1), 83–94.

14 K. Lee, A. J. Heeger and Y. Cao, Reflectance of polyaniline protonated with camphor sulfonic acid: disordered metal on the metal-insulator boundary, *Phys. Rev. B: Condens. Matter Mater. Phys.*, 1993, **48**(20), 14884.

15 L. A. A. Pettersson, F. Carlsson, O. Inganäs and H. Arwin, Spectroscopic ellipsometry studies of the optical properties of doped poly(3,4-ethylenedioxythiophene): an anisotropic metal, *Thin Solid Films*, 1998, **313**, 356–361.

16 Y. Du, X. Cui, L. Li, H. Tian, W. X. Yu and Z. X. Zhou, Dielectric Properties of DMSO-Doped-PEDOT:PSS at THz Frequencies, *Phys. Status Solidi B*, 2017, **255**(4), 1700547.

17 N. V. Smith, Classical generalization of the Drude formula for the optical conductivity, *Phys. Rev. B: Condens. Matter Mater. Phys.*, 2001, **64**(15), 155106.

18 S. A. Maier, *Plasmonics: fundamentals and applications*, Springer Science & Business Media, 2007.

19 M. Fox, *Optical properties of solids*, Oxford University Press, 2nd edn, 2010.

20 K. Lee, S. Cho, S. H. Park, A. J. Heeger, C.-W. Lee and S.-H. Lee, Metallic transport in polyaniline, *Nature*, 2006, **441**(7089), 65.

21 K. Lee and A. J. Heeger, Optical reflectance studies of conducting polymers on the metal-insulator boundary, *Synth. Met.*, 1997, **84**(1–3), 715–718.

22 Y. Chang, K. Lee, R. Kiebooms, A. Aleshin and A. J. Heeger, Reflectance of conducting poly(3,4-ethylenedioxythiophene), *Synth. Met.*, 1999, **105**(3), 203–206.

23 K. Lee, R. Menon, C. O. Yoon and A. J. Heeger, Reflectance of conducting polypyrrole: observation of the metal-insulator transition driven by disorder, *Phys. Rev. B: Condens. Matter Mater. Phys.*, 1995, **52**(7), 4779.

24 K. Lee, A. J. Heeger and Y. Cao, Reflectance spectra of polyaniline, *Synth. Met.*, 1995, **72**(1), 25–34.

25 N. Kim, B. H. Lee, D. Choi, G. Kim, H. Kim and J.-R. Kim, *et al.*, Role of interchain coupling in the metallic state of conducting polymers, *Phys. Rev. Lett.*, 2012, **109**(10), 106405.

26 R. S. Kohlman, J. Joo, Y. G. Min, A. G. MacDiarmid and A. J. Epstein, Crossover in electrical frequency response through an insulator-metal transition, *Phys. Rev. Lett.*, 1996, **77**(13), 2766.

27 R. S. Kohlman, J. Joo, Y. Z. Wang, J. P. Pouget, H. Kaneko and T. Ishiguro, *et al.*, Drude metallic response of polypyrrole, *Phys. Rev. Lett.*, 1995, **74**(5), 773.

28 R. S. Kohlman, A. Zibold, D. B. Tanner, G. G. Ihas, T. Ishiguro and Y. G. Min, *et al.*, Limits for metallic conductivity in conducting polymers, *Phys. Rev. Lett.*, 1997, **78**(20), 3915.

29 K. Lee, E. K. Miller, A. N. Aleshin, R. Menon, A. J. Heeger and J. H. Kim, *et al.*, Nature of the metallic state in conducting polypyrrole, *Adv. Mater.*, 1998, **10**(6), 456–459.

30 L. A. A. Pettersson, T. Johansson, F. Carlsson, H. Arwin and O. Inganäs, Anisotropic optical properties of doped poly(3,-ethylenedioxythiophene), *Synth. Met.*, 1999, **101**(1–3), 198–199.

31 M. Schubert, C. Bundesmann, H. v. Wenckstern, G. Jakopic, A. Haase and N. K. Persson, *et al.*, Carrier redistribution in organic/inorganic (poly(3,4-ethylenedioxy thiophene/poly(styrene-sulfonate)polymer)-Si) heterojunction determined from infrared ellipsometry, *Appl. Phys. Lett.*, 2004, **84**(8), 1311–1313.

32 M. Schubert, C. Bundesmann, G. Jakopic, H. Maresch, H. Arwin and N. C. Persson, *et al.*, Infrared ellipsometry characterization of conducting thin organic films, *Thin Solid Films*, 2004, **455**, 295–300.

33 M. Schubert, *Infrared Ellipsometry on Semiconductor Layer Structures: Phonons, Plasmons, and Polaritons*, Springer, 2004.

34 H. Fujiwara, *Spectroscopic ellipsometry: principles and applications*, John Wiley & Sons, 2007.

35 L. A. A. Pettersson, S. Ghosh and O. Inganäs, Optical anisotropy in thin films of poly(3,4-ethylenedioxythiophene)–poly(4-styrenesulfonate), *Org. Electron.*, 2002, **3**(3–4), 143–148.

36 D. Farka, H. Coskun, J. Gasiorowski, C. Cobet, K. Hingerl and L. M. Uiberlacker, *et al.*, Anderson-Localization and the Mott–Ioffe–Regel Limit in Glassy-Metallic PEDOT, *Adv. Electron. Mater.*, 2017, **3**(7), 1700050.

37 J. Gasiorowski, R. Menon, K. Hingerl, M. Dachev and N. S. Sariciftci, Surface morphology, optical properties and conductivity changes of poly(3,4-ethylenedioxythiophene):poly-(styrenesulfonate) by using additives, *Thin Solid Films*, 2013, **536**, 211–215.

38 A. Laskarakis, V. Karagkiozaki, D. Georgiou, C. Gravalidis and S. Logothetidis, Insights on the Optical Properties of Poly(3,4-Ethylenedioxythiophene):Poly(Styrenesulfonate) Formulations by Optical Metrology, *Materials*, 2017, **10**(8), 959.

39 A. Laskarakis, P. G. Karagiannidis, D. Georgiou, D. M. Nikolaidou and S. Logothetidis, Optical investigations of the effect of solvent and thermal annealing on the optoelectronic properties of poly(3,4-ethylenedioxythiophene):poly(styrenesulfonate) films, *Thin Solid Films*, 2013, **541**, 102–106.

40 P. Kühne, N. Armakavicius, V. Stanishev, C. M. Herzinger, M. Schubert and V. Darakchieva, Advanced Terahertz Frequency-Domain Ellipsometry Instrumentation for In Situ and Ex Situ Applications, *IEEE Trans. Terahertz Sci. Technol.*, 2018, **8**(3), 257–270.

41 P. Kühne, C. M. Herzinger, M. Schubert, J. A. Woollam and T. Hofmann, Invited Article: An integrated mid-infrared, far-infrared, and terahertz optical Hall effect instrument, *Rev. Sci. Instrum.*, 2014, **85**(7), 071301.

42 T. Hofmann, C. M. Herzinger, A. Boosalis, T. E. Tiwald, J. A. Woollam and M. Schubert, Variable-wavelength frequency-domain terahertz ellipsometry, *Rev. Sci. Instrum.*, 2010, **81**(2), 023101.

43 M. M. Junda, A. B. Phillips, R. R. Khanal, M. J. Heben and N. J. Podraza, Determination of conductivity anisotropy and the role of doping in single walled carbon nanotube thin films with THz spectroscopic ellipsometry, *Carbon*, 2018, **129**, 592–597.

44 O. Bubnova, Z. U. Khan, A. Malti, S. Braun, M. Fahlman and M. Berggren, *et al.*, Optimization of the thermoelectric figure of merit in the conducting polymer poly(3,4-ethylenedioxythiophene), *Nat. Mater.*, 2011, **10**(6), 429.

45 O. Bubnova, Z. U. Khan, H. Wang, S. Braun, D. R. Evans and M. Fabretto, *et al.*, Semi-metallic polymers, *Nat. Mater.*, 2014, **13**(2), 190.

46 G.-H. Kim, L. Shao, K. Zhang and K. P. Pipe, Engineered doping of organic semiconductors for enhanced thermoelectric efficiency, *Nat. Mater.*, 2013, **12**(8), 719.

47 B. Cho, K. S. Park, J. Baek, H. S. Oh, Y.-E. Koo Lee and M. M. Sung, Single-crystal poly(3,4-ethylenedioxythiophene) nanowires with ultrahigh conductivity, *Nano Lett.*, 2014, **14**(6), 3321–3327.

48 N. Kim, B. Lee, D. Choi, G. Kim, H. Kim and J.-R. Kim, *et al.*, Role of Interchain Coupling in the Metallic State of Conducting Polymers, *Phys. Rev. Lett.*, 2012, **109**(10), 106405.

49 O. Bubnova, Z. Khan, H. Wang, S. Braun, D. R. Evans and M. Fabretto, *et al.*, Semi-metallic polymers, *Nat. Mater.*, 2013, **13**(2), nmat3824.

50 Y. H. Kim, C. Sachse, M. L. Machala, C. May, L. Müller-Meskamp and K. Leo, Highly Conductive PEDOT:PSS Electrode with Optimized Solvent and Thermal Post-Treatment for ITO-Free Organic Solar Cells, *Adv. Funct. Mater.*, 2011, **21**(6), 1076–1081.

51 F. Yan, E. P. J. Parrott, B. S. Y. Ung and E. Pickwell-MacPherson, Solvent doping of PEDOT/PSS: effect on terahertz optoelectronic properties and utilization in terahertz devices, *J. Phys. Chem. C*, 2015, **119**(12), 6813–6818.

52 H. Bednarski, B. Hajduk, J. Jurusik, B. Jarząbek, M. Domański and K. Łaba, *et al.*, The Influence of PEDOT to PSS Ratio on the Optical Properties of PEDOT:PSS Thin Solid Films-Insight from Spectroscopic Ellipsometry, *Acta Phys. Pol., A*, 2016, **130**(5), 1242–1244.

53 M. Yamashita, C. Otani, M. Shimizu and H. Okuzaki, Effect of solvent on carrier transport in poly(3,4-ethylenedioxythiophene)/poly(4-styrenesulfonate) studied by terahertz and infrared-ultraviolet spectroscopy, *Appl. Phys. Lett.*, 2011, **99**(14), 213.

54 M. V. Fabretto, D. R. Evans, M. Mueller, K. Zuber, P. Hojati-Talemi and R. D. Short, *et al.*, Polymeric material with metal-like conductivity for next generation organic electronic devices, *Chem. Mater.*, 2012, **24**(20), 3998–4003.

55 R. M. A. Azzam and N. M. Bashara, *Ellipsometry and polarized light: North-Holland. Sole distributors for the USA and Canada*, Elsevier Science Publishing Co., Inc., 1987.

56 N. W. Ashcroft and N. D. Mermin, *Solid State Physics*, Holt, Rinehart and Winston, 1976.

57 C. M. Wolfe, N. Holonyak Jr and G. E. Stillman, *Physical properties of semiconductors*, Prentice-Hall, Inc., 1988.

58 N. Mott, *Metal-Insulator Transitions*, Taylor & Francis, 1990.

59 N. F. Mott, Metal-insulator transition, *Rev. Mod. Phys.*, 1968, **40**(4), 677.

60 G. Bergmann, Weak localization in thin films: a time-of-flight experiment with conduction electrons, *Phys. Rep.*, 1984, **107**(1), 1–58.

61 T.-T. Kang, M. Yamamoto, M. Tanaka, A. Hashimoto, A. Yamamoto and R. Sudo, *et al.*, Terahertz characterization of semiconductor alloy AlInN: negative imaginary conductivity and its meaning, *Opt. Lett.*, 2009, **34**(16), 2507–2509.

62 T. L. Cocker, D. Baillie, M. Buruma, L. V. Titova, R. D. Sydora and F. Marsiglio, *et al.*, Microscopic origin of the Drude-Smith model, *Phys. Rev. B*, 2017, **96**(20), 205439.

63 O. Bubnova, Z. U. Khan, A. Malti, S. Braun, M. Fahlman and M. Berggren, *et al.*, Optimization of the thermoelectric figure of merit in the conducting polymer poly(3,4-ethylenedioxythiophene), *Nat. Mater.*, 2011, **10**(6), 429–433.

64 J. Hwang, I. Schwendeman, B. C. Ihas, R. J. Clark, M. Cornick and M. Nikolou, *et al.*, In situ measurements

of the optical absorption of dioxythiophene-based conjugated polymers, *Phys. Rev. B: Condens. Matter Mater. Phys.*, 2011, **83**(19), 195121.

65 J. Hwang, D. B. Tanner, I. Schwendeman and J. R. Reynolds, Optical properties of nondegenerate ground-state polymers: Three dioxythiophene-based conjugated polymers, *Phys. Rev. B: Condens. Matter Mater. Phys.*, 2003, **67**(11), 115205.

66 K. E. Aasmundtveit, E. J. Samuelsen, L. A. A. Pettersson, O. Ingans, T. Johansson and R. Feidenhans'l, Structure of thin films of poly(3,4-ethylenedioxythiophene), *Synth. Met.*, 1999, **101**(1), 561–564.

67 A. M. Nardes, M. Kemerink and R. A. J. Janssen, Anisotropic hopping conduction in spin-coated PEDOT:PSS thin films, *Phys. Rev. B: Condens. Matter Mater. Phys.*, 2007, **76**(8), 085208.

68 A. M. Nardes, M. Kemerink, R. A. J. Janssen, J. A. M. Bastiaansen, N. M. M. Kiggen and B. M. W. Langeveld, *et al.*, Microscopic understanding of the anisotropic conductivity of PEDOT:PSS thin films, *Adv. Mater.*, 2007, **19**(9), 1196–1200.

69 S.-I. Na, G. Wang, S.-S. Kim, T.-W. Kim, S.-H. Oh and B.-K. Yu, *et al.*, Evolution of nanomorphology and anisotropic conductivity in solvent-modified PEDOT:PSS films for polymeric anodes of polymer solar cells, *J. Mater. Chem.*, 2009, **19**(47), 9045–9053.

70 J. Edberg, D. Iandolo, R. Brooke, X. J. Liu, C. Musumeci and J. W. Andreasen, *et al.*, Patterning and Conductivity Modulation of Conductive Polymers by UV Light Exposure, *Adv. Funct. Mater.*, 2016, **26**(38), 6950–6960.

71 F. Zhang, H. W. Wang, K. Tominaga, M. Hayashi, T. Hasunuma and A. Kondo, Application of THz Vibrational Spectroscopy to Molecular Characterization and the Theoretical Fundamentals: An Illustration Using Saccharide Molecules, *Chem. – Asian J.*, 2017, **12**(3), 324–331.

72 A. Elfwing, C. S. Ponseca Jr, L. Ouyang, A. Urbanowicz, An Krotkus and D. Tu, *et al.*, Conducting Helical Structures from Celery Decorated with a Metallic Conjugated Polymer Give Resonances in the Terahertz Range, *Adv. Funct. Mater.*, 2018, 1706595.